npj | parkinson's disease

Article

Published in partnership with the Parkinson's Foundation

https://doi.org/10.1038/s41531-025-01020-0

Multiparametric quantitative MRI uncovers putamen microstructural changes in Parkinson's disease

Elior Drori [1] ✉, Lee Cohen[1], David Arkadir[2,3], Gilad Yahalom[3,4,5] & Aviv A. Mezer[1,5]

Parkinson's disease (PD) is a progressive neurodegenerative disorder dominated by motor and non-motor dysfunction. Despite extensive research, in vivo characterization of PD-related brain microstructure remains a challenge, limiting diagnostic and therapeutic advances. The putamen, a subcortical region crucial for movement regulation, is prominently affected in early PD. Here, we collected multiparametric quantitative MRI (qMRI) data from PD patients and healthy controls, to investigate biophysical alterations in the putamen. Gradient analysis revealed significant spatial variation and interhemispheric asymmetries in biophysical properties – including relaxation rates (R1, R2, R2*), water fraction (WF), susceptibility, MTsat, and diffusion metrics (MD, FA) – along its anterior-posterior axis. PD patients showed altered gradients, particularly increased WF in the posterior putamen, suggesting tissue atrophy or neuroinflammation, and correlating with motor symptom laterality. Our findings highlight the posterior putamen as a PD pathology hotspot and demonstrate the potential of qMRI gradient analysis for detecting clinically relevant brain changes.

Parkinson's Disease (PD) is a progressive neurodegenerative disorder primarily characterized by motor and non-motor symptoms, fundamentally altering the life quality of those affected. Despite extensive research, the microstructural neural changes associated with PD have not yet been fully characterized in vivo. This limits the ability to monitor the pathophysiological mechanisms of the disease, and consequently hinders the research and development of more effective diagnostic and therapeutic strategies[1].

The putamen, primarily associated with the motor domain of the striatum, is a key brain structure within the basal ganglia, which plays a crucial role in regulating movement and facilitating goal-directed behavior[2]. In PD, the progressive loss of dopaminergic neurons in the substantia nigra pars compacta leads to a significant decrease in dopamine input to the putamen. This depletion disrupts the dopaminergic circuitry, impairing cellular processes such as synaptic plasticity and neurotransmitter regulation within the putamen[3]. These changes lead to degeneration of the putamen as reflected by alterations in its biophysical and cellular composition, including iron deposition, myelin integrity, and macromolecular content[4,5]. Consequently, the functionality of the putamen is impaired, giving rise to the characteristic motor symptoms of PD[2].

Motor impairment severity in PD, typically assessed through MDS-Unified Parkinson's Disease Rating Scale Part III (MDS-UPDRS III), has been associated with biophysical alterations in the putamen[6–8]. Previous research has further highlighted two spatial aspects of putamen neurodegeneration in PD. One key aspect found using PET and SPECT is a gradual dopamine depletion starting in the posterior parts and advancing anteriorly with PD progression[9,10]. Furthermore, an MRI study found that the major anatomical axis of the putamen, i.e., its anterior-posterior (AP) axis, is associated with spatial microstructural patterns that undergo alterations in the posterior region during the early stages of PD[11]. Another key property is inter-hemispheric asymmetry; PET, SPECT and MRI studies have demonstrated asymmetry in dopamine depletion and tissue microstructure integrity, corresponding contralaterally with the asymmetrical motor signs commonly seen in early PD stages[2,10,11].

These findings in PD are in line with the view of inherent spatial inhomogeneities of the healthy striatum and particularly the putamen. Animal and postmortem human studies found molecular and connectivity gradients in the healthy striatum, using histochemical staining and neural tracing methods[12–14]. Furthermore, in vivo human studies have identified gradients of connectivity, function and biophysical properties along the major axes of the striatum, using diffusion MRI tractography, task-based functional MRI (fMRI), resting-state fMRI, and quantitative MRI (qMRI)[11,15–21].

[1]Edmond and Lily Safra Center for Brain Sciences, The Hebrew University of Jerusalem, Jerusalem, Israel. [2]Department of Neurology, Hadassah Medical Center, Jerusalem, Israel. [3]School of Medicine, The Hebrew University of Jerusalem, Jerusalem, Israel. [4]Department of Neurology and the Movement Disorders Unit, Shaare Zedek Medical Center, Jerusalem, Israel. [5]These authors contributed equally: Gilad Yahalom, Aviv A. Mezer.
✉e-mail: elior.drori@mail.huji.ac.il

Recent advances in neuroimaging, particularly multiparametric qMRI, have opened new avenues for exploring the brain's microstructure in vivo[22,23]. qMRI encompasses a range of imaging techniques that quantify the physical properties of brain tissue, and has been shown to be sensitive to different aspects of local microstructural environment, such as myelination, iron and cellular membranes[23]. As a result, qMRI has become instrumental in detecting subtle biological changes in development, normal aging and neurodegenerative diseases, particularly in PD[23,24]. Key qMRI parameters include R1 (longitudinal relaxation rate), R2 (transverse relaxation rate), and R2* (effective transverse relaxation rate), which are sensitive to tissue macromolecular composition and iron content[23,25,26]. Quantitative susceptibility mapping (QSM) offers information on tissue magnetism and iron deposition[23,25], while Magnetization Transfer Saturation (MTsat) indicates the exchange between free and bound protons, which depends on the macromolecular environment[23,27]. Water Fraction, another qMRI metric, helps in understanding tissue hydration[23,28]. Furthermore, Mean Diffusivity (MD) and Fractional Anisotropy (FA), derived from Diffusion Tensor Imaging (DTI), provide information on the diffusion of water molecules, indicating the tissue structure and integrity[29,30]. The linear co-dependency of different qMRI metrics (termed relaxivity) were suggested to provide sensitivity to the molecular composition and iron homeostasis in the tissue[26,31].

In recent years, several potential disease-modifying drugs have shown promising evidence of neuroprotection[32–34]. Therefore, accurate diagnosis of PD and monitoring disease progression during studies involving these drugs are crucial for drawing meaningful conclusions about disease modification. qMRI may offer valuable insights into addressing this challenge.

In this study, we hypothesized that different biophysical properties of the putamen exhibit distinct spatial variations (i.e., gradients) along the AP axis. We further hypothesized that PD-related changes in these spatial gradients correlate with clinical symptom patterns, particularly motor signs. To test these hypotheses, we acquired a comprehensive multiparametric qMRI dataset, in order to characterize spatial biophysical gradients, in vivo, and assess their potential as biomarkers for PD-related neurodegeneration. Specifically, we aimed to analyze variations in relaxation rates, WF, susceptibility, MTsat, and diffusion parameters along the AP axis of the putamen, measured on the same subjects, in both PD and healthy controls (HC).

By employing a spatial gradient analysis method developed in recent research[11], we sought to obtain a comprehensive, multi-dimensional view of the qMRI variations in the putamen associated with PD. This view may provide a deeper understanding of the biophysical changes in PD and their association with clinical manifestations. Ultimately, our study highlights the potential of advanced localized gradient analysis in qMRI as a sensitive tool for tracking subtle neurodegenerative changes, which may aid future efforts in diagnostic and therapeutic monitoring of PD and other neurodegenerative diseases.

Results

Demographics

PD patients ($n = 62$) did not statistically differ from HC ($n = 28$) in age (Two-sample t test, $t(88) = -0.68$, $P = 0.50$) or sex (Pearson's $\chi^2(88) = -2.11$, $P = 0.15$). MDS-UPDRS III score was significantly higher in PD ($t(83) = 11.29$, $P < 10^{-17}$), reflecting the presence of motor signs in PD. The Montreal Cognitive Assessment (MoCA) score was significantly lower in PD ($t(85) = -4.29$, $P < 0.00005$), indicating lower cognitive function in PD. The demographics and PD characteristics are shown in Table 1.

Table 1 | Demographics and PD characteristics

Variable	PD ($n = 62$)	HC ($n = 28$)
Age, years	68.4 ± 10.1 (range, 37–86)	69.9 ± 8.3 (range, 49–78)
Sex, female, *n* (%)	21 (34%)	14 (50%)
Disease duration, years	5.3 ± 4.3 (range, 0–21)	NA
H&Y scale	2.1 ± 0.8	NA
MDS-UPDRS III, score	29.8 ± 11.7 (range, 10–69)	3.3 ± 3.4 (range, 0–15)
Age, years	68.4 ± 10.1 (range, 37–86)	69.9 ± 8.3 (range, 49–78)

H&Y Hoehn and Yahr scale of PD progression. For further details, see Methods.

Multiparametric Biophysical Gradients in the putamen

Multiparametric quantitative mapping of the participants included whole-brain R1, R2, R2*, WF, MTsat, susceptibility, MD and FA maps (Fig. 1). Our multiparametric analysis along the AP axis of the putamen has revealed distinct spatial variations in different biophysical parameters. Employing linear mixed-effects models (LMMs) covarying for Age and Sex, we identified gradients of relaxation rates R1, R2, and R2*, WF, susceptibility, MTsat, and dMRI parameters MD and FA. These findings, depicted in Fig. 2 and further detailed in Supplementary Table 1, align with previous research, replicating findings in WF, R1, and R2* and extending it to additional parameters[11].

Notably, R1, R2, R2*, susceptibility, MTsat and FA showed generally common spatial patterns with values increasing towards posterior regions, and some decreases at the most posterior positions. WF and MD exhibited decreasing values toward posterior positions, followed by an increase at the posterior-most positions. This inverse behavior of WF and MD, compared to other parameters, is expected due to their opposing dependency on the tissue water content (see Discussion). Despite observed differences, all gradients were spatially intercorrelated, as depicted in Supplementary Fig. 1.

To assess the nature of the observed spatial nonlinearities, we further expanded our analysis to include a nonlinear approach. Specifically, we repeated our LMM analysis while incorporating a quadratic Position term. Interestingly, this approach yielded statistically significant quadratic change in all MRI parameters, suggesting a non-linear aspect to their spatial variations (Supplementary Note 1 and Supplementary Fig. 2). While the quadratic term adds a layer of complexity that captures more nuanced spatial dynamics, we have opted to focus our interpretation and discussion on the linear approach, which is grounded in its simplicity and interpretability, and provides a balance between analytical rigor and practical understandability of later group analyses.

Biophysical gradient changes in Parkinson's disease

Intriguingly, the putamen gradients of several parameters differed between PD and HC, evidenced by interaction effects between the Clinical Group and Spatial Position in the LMM analysis (Fig. 2 and Supplementary Table 1). Relatively large and highly significant interaction effects were found in the gradients of WF ($\beta_{PD} = 0.46$, 95% CI = [0.33, 0.59], $P < 10^{-10}$) and R2* ($\beta_{PD} = -0.47$, 95% CI = [−0.63, -0.32], $P < 10^{-7}$). In addition, significant differences were also found in the gradients of R1 ($\beta_{PD} = -0.2$, 95% CI = [−0.35, −0.05], $P = 0.022$), MTsat ($\beta_{PD} = -0.2$, 95% CI = [−0.33, −0.07], $P = 0.008$), and FA ($\beta_{PD} = -0.28$, 95% CI = [−0.48, −0.08], $P = 0.019$). These interaction effects indicated less steep gradient slopes in PD compared to HC. However, power analyses for the interaction effects confirmed sufficient statistical power only for the larger effects found using WF and R2* (see Supplementary Note 2).

Beyond PD-related changes, we found statistically significant main effects of Age in WF ($\beta = -0.24$, 95% CI = [−0.43 −0.05], $P = 0.031$), and MTsat ($\beta = -0.25$, 95% CI = [−0.41 −0.09], $P = 0.008$). In R2*, we found marginally significant main effects of Age ($\beta = 0.19$, 95% CI = [0.02, 0.36], uncorrected-$P = 0.03$), and Sex ($\beta_{male} = -0.41$, 95% CI = [−0.76, −0.05], uncorrected-$P = 0.025$).

Post hoc analysis (see Methods) localized the maximal gradient differences between PD and HC in R1, WF, R2*, R2, MD, and FA to the posterior putamen (PP), specifically at position 0.85/1.00 along the AP axis. The maximal gradient changes in Susceptibility and MTsat were observed more anteriorly, at positions 0.60/1.00 and 0.45/1.00, respectively. However, only WF and R2* local gradient changes were found significant (WF: 0.75–1.00/1.00; R2*: 0.80–0.95/1:00; see Fig. 3). Notably, traditional volumetric and median value analyses of the entire putamen failed to detect group differences, as shown in Supplementary Fig. 3. Our results support

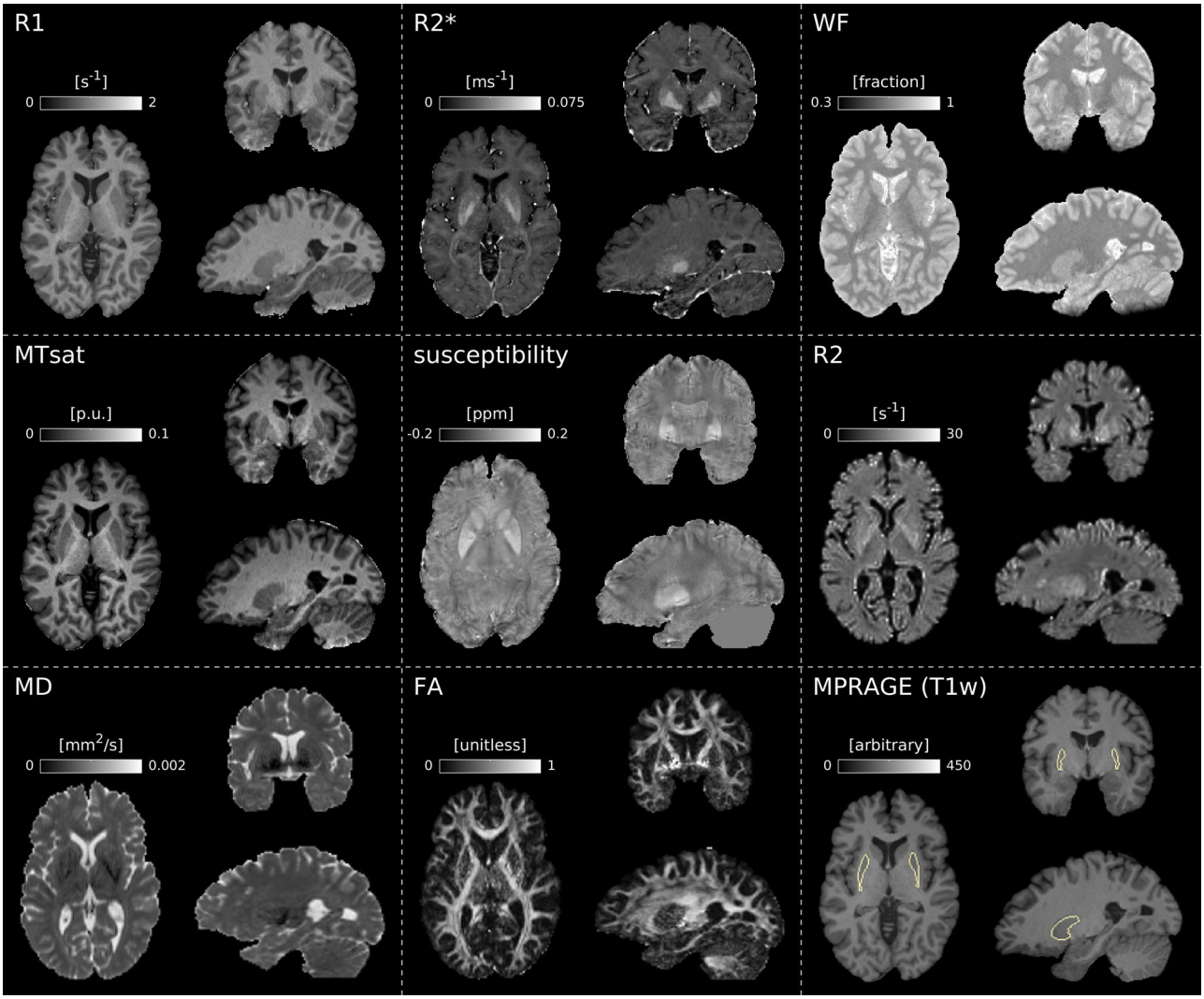

Fig. 1 | Multiparametric qMRI mapping of a single subject. A single HC subject's axial, coronal and sagittal brain slices of 3-dimensional qMRI and dMRI maps: R1, R2*, WF, MTsat, susceptibility, R2, MD, and FA. These maps collectively provide a multidimensional view of the brain's microstructural and biophysical properties. Bottom-right panel: An anatomical MPRAGE T1w image; the putamen ROI is outlined (yellow).

previous findings of PP alterations in PD[9–11] and underscores the value of localized gradient analysis in revealing subtle microstructural variations.

Motor symptoms and biophysical changes

To investigate the behavioral relevance of the biophysical alterations identified in PD, we examined associations between WF and R2* gradients and both overall motor severity (MDS-UPDRS III score) and motor body-side asymmetry. No statistically significant correlations were found between motor severity and qMRI values along the putamen AP axis, or within the whole putamen. A non-robust effect was observed, but it depended on the WF scaling method and on an outlier subject (see details in Supplementary Note 3 and Supplementary Figs. 4, 5).

By contrast, in patients with motor sign asymmetries ($n = 45$; see Methods), WF was significantly higher in the most-affected side (MAS), compared to the less-affected side (LAS). This effect was spatially dependent, predominantly located in posterior positions (0.65–0.70/1.00), suggesting increased tissue water content in the affected PP (Fig. 4A). No significant differences in R2* gradients were observed between MAS and LAS, suggesting no detectable inter-hemispheric variation in iron content (Supplementary Fig. 6A).

Consistent with these findings, inter-hemispheric asymmetry in the PP was significantly correlated with motor asymmetry. Specifically, we found a significant correlation between WF asymmetry and motor symptom asymmetry score, with higher WF associated with contralateral symptoms (Fig. 4B). In contrast, R2* asymmetry did not show a significant correlation with motor asymmetry (Supplementary Fig. 6B). Importantly, whole-putamen analysis failed to detect MAS-LAS differences or correlation with motor asymmetry. Our findings align with previous results[11] and may suggest that motor symptom laterality in PD is primarily associated with increased water fraction in the contralateral PP rather than variations in iron concentration.

Beyond motor function, WF values in the putamen showed marginal correlations with MoCA scores, particularly in anterior positions along the AP axis, which are more associated with cognitive function[15]. However, these correlations were not robust and depended on the WF calibration method and the presence of outlier subjects (Supplementary Note 4 and Supplementary Figs. 7, 8). No significant correlations were observed between R2* and MoCA scores.

Finally, Tissue- and Iron-Relaxivity analyses (dR1/d(1-WF) and dR1/dR2*; see Methods) revealed no statistically significant differences between PD and HC in the PP (Mann-Whitney U tests, $P > 0.14$), suggesting no detectable PD-related changes in macromolecular compositions or in iron homeostasis, as distinct from tissue content.

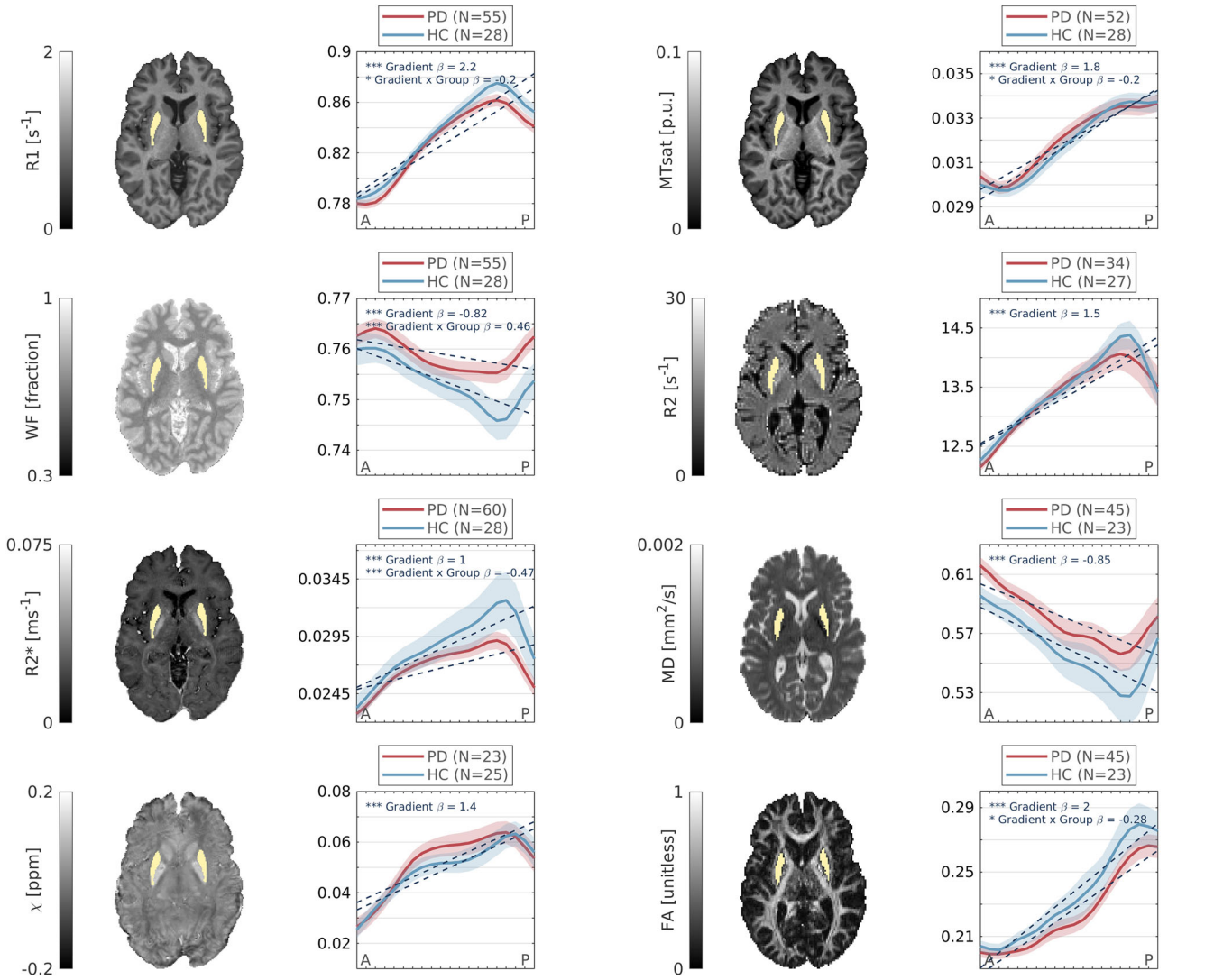

Fig. 2 | Putamen AP multiparametric gradients uncover local biophysical changes in PD. Spatial profiles of various biophysical mappings along the AP axis of the putamen uncover distinct and statistically significant gradients, as well as interactions with PD (Linear Mixed-effect models). Gradients of R1, WF, R2*, susceptibility (χ), MTsat, R2, MD and FA shown are averaged across the left and right putamen. Shaded area represents ± 1 SEM. Dashed lines represent the model's linear fit. Standardized coefficient estimates (β) of spatial effect from anterior to posterior and PD group interaction are shown. *$P < 0.05$; ***$P < 0.0000001$ (corrected using BH-FDR). Axial brain slices of a representative HC subject are shown for each parameter, with bilateral putamen masks.

Discussion

Our study leveraged qMRI and spatial gradient approach to investigate the putamen, revealing deep brain biophysical changes in both healthy individuals and PD patients. These investigations have provided several critical insights. Firstly, our findings confirmed the existence of biophysical spatial gradients within the putamen, corroborating the concept of striatal gradients and demonstrating the capability of MRI to capture these spatial variations in a living brain. This supports the notion that the putamen's tissue microstructure varies systematically along its AP axis, which has implications for understanding its functional organization and connectivity in both health and disease.

Secondly, we identified localized neurodegenerative changes in the PP, predominantly related to water increase in PD patients. These alterations were confined to the posterior positions 0.80–1.00/1.00 along the AP axis, with maximal difference at 0.85/1.00.

This finding is particularly significant as it aligns with the hypothesis that PD pathology initiates in specific brain regions and progresses in a spatially structured manner. Our results add to the growing body of evidence suggesting that the PP may be a critical site for early PD-related changes, further emphasizing the importance of spatially resolved analyses in detecting and understanding the progression of neurodegenerative diseases.

Lastly, our study established a link between changes in tissue water in the PP and clinical aspects of PD. Asymmetry in water content within the PP was associated with the lateralization of motor symptoms, corroborating earlier results in clinical MRI[11], PET and SPECT[10]. This correlation underscores the functional relevance of the observed microstructural alterations, indicating that the side of the brain exhibiting more severe tissue loss is associated with more pronounced motor impairment on the opposite side of the body. Such findings highlight the potential of qMRI to provide biomarkers that not only reflect the underlying neuropathology of PD but also correlate with clinical manifestations of the disease, offering a more integrated view of brain structure and function. Beside motor aspects of PD, we observed a weak association between WF in the putamen and cognitive impairment, assessed through MoCA. However, this result depended on outlier subjects and was not robust to WF scaling method, warranting cautious interpretation.

While all qMRI metrics showed spatial correlation, they differed in their capacity to demonstrate PD-related alterations. Specifically, R1, WF, R2*, MTsat and FA showed reduced AP gradients in PD, compared to HC.

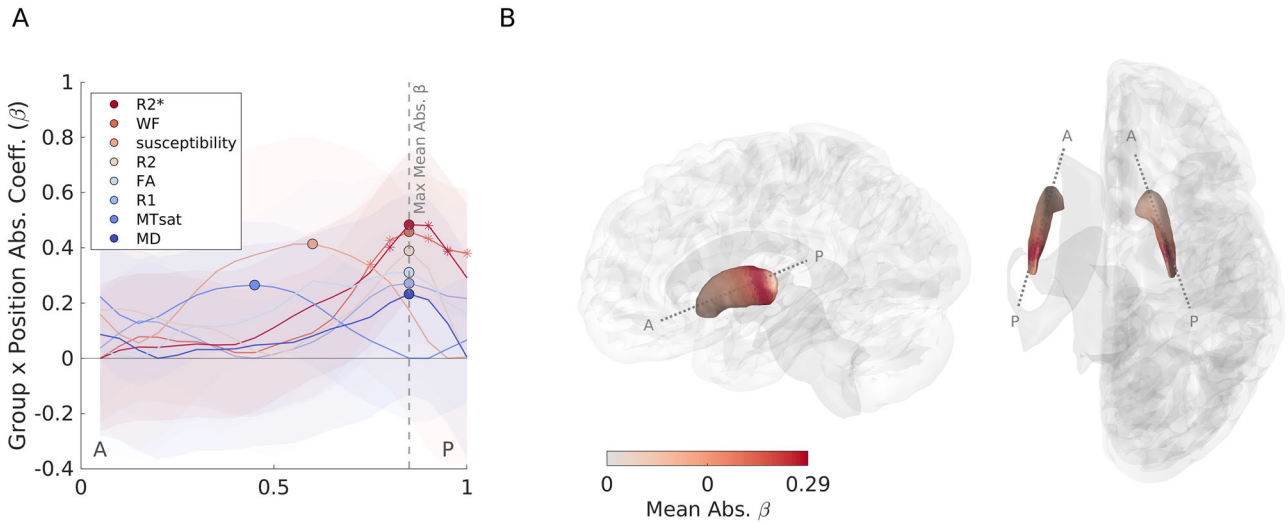

Fig. 3 | Gradient change in PD is consistently maximal at the PP. A Absolute standardized coefficient estimates (β) for the Clinical Group × Position interaction effect, separate for each position (see Methods), are plotted along the AP axis for each qMRI parameter. The maximal β values for R1, WF, R2*, R2, MD and FA (closed circles), as well as the maximal average β across all parameters (dashed line), are observed at the posterior position 0.84/1.00. Significant effects in WF and R2* are detected around this position, within the range of 0.75–1.00/1.00. Asterisks indicate BH-FDR corrected $P < 0.05$. Shaded areas represent 95% confidence intervals. **B** The Absolute β values for the Clinical Group × Position interaction, averaged across qMRI parameters are visualized along the AP axis of the putamen. The maximum value ($\beta = 0.29$) is located at the posterior position 0.84/1.00.

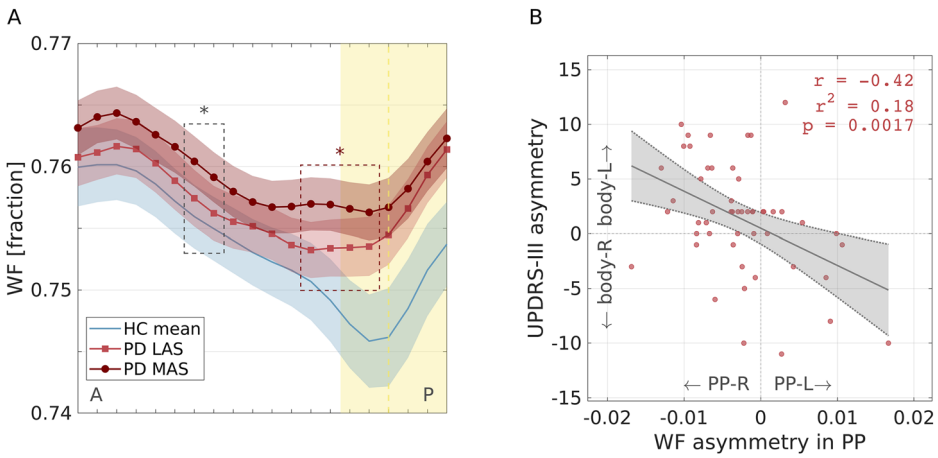

Fig. 4 | WF asymmetry in PP is associated with contralateral motor signs. A WF gradients in the putamen of patients with motor body-side predominance ($n = 46$ having motor asymmetry) and healthy controls. PD gradients are grouped into LAS and MAS, based on patients' contralateral motor laterality. Yellow patch and dashed line represent significant and maximal PD-HC gradient change, respectively (see Fig. 3). Asterisks represent significant differences between LAS and MAS, using paired t-tests ($P < 0.05$, corrected for multiple comparisons; normality was verified prior to testing; see Methods). Posterior significant positions (marked in red rectangle) are used for computing the PP WF asymmetry displayed in (**B**). **B** WF asymmetry between left and right PP in PD patients ($n = 52$ with available UPDRS III data) is significantly correlated with contralateral motor signs asymmetry. PP positions used in this analysis are those marked in red rectangle in (**A**). Pearson's $r = -0.42$; $r^2 = 0.18$; $P = 0.0017$.

Notably, all qMRI parameters are sensitive to the water content. The substantial effect found in WF and its association with PD motor signs, along with smaller effects in other parameters, suggest that the primary source of PD-related changes in the PP is water content. Additionally, the absence of statistically significant changes on both the macroscale (volumetric differences), and the molecular scale (tissue and iron relaxivities), supports the conclusion that the variations in the PP reflect micro- or mesoscale alterations. Specifically, the increased water content may be attributed to reduced non-water cellular and axonal tissue[31], as well as to neuroinflammation processes which involve elevation of extracellular water content[35].

We found a spatially dependent decrease in R2* in PD, characterized by a less pronounced gradient slope. Contrary to expectations of increased R2* and QSM in the basal ganglia in PD due to iron deposition, previous literature has presented mixed results, with studies finding reduced postmortem iron levels in the putamen in PD[36], or insignificant differences between PD and HC in the putamen or PP, using either R2* or QSM[37–41]. Importantly, while R2* is commonly correlated with iron content, it is also influenced by other factors such as myelin content, fiber orientation, calcium, tissue integrity, vascularization, and water content[42]. Thus, it is possible that increased water content has an opposite effect on the R2* measurement.

Our study builds on findings from previous work, which identified an AP gradient change in the putamen with normal aging using qMRI (R1, WF, and R2*) and in PD using semi-quantitative MRI data (T1w/T2w ratio)[11]. Here, we replicate and extend these findings in PD using multiparametric qMRI, suggesting that the observed changes are primarily due to variations in water content. Although our data were acquired on a specific MRI scanner (Siemens) and field strength (3 T), prior study demonstrated that similar gradient patterns were reproducible across three independent qMRI datasets from healthy subjects scanned on different MRI systems (Siemens, Philips, GE) and field strengths (3 T and 7 T). While nuclear

imaging data (e.g., DATSCAN) are not available in this dataset, limiting direct conclusions regarding the relationship between our measurements and dopaminergic changes in the nigrostriatal system, the previous study indicated a potential link. Specifically, it reported a correlation between DAT and T1w/T2w asymmetries in the PP, explaining 25% of the variance, which suggests an association between qMRI-detected tissue alterations in the PP and dopaminergic loss.

Our study faces several limitations that merit consideration. Firstly, the comprehensive qMRI battery required for detailed microstructural analysis necessitated long scanning sessions, approximately 1.5 h, posing challenges for subjects. This extensive scan time led to variability in the completion rates of different qMRI parameters, as well as motion artifacts, resulting in varied sample sizes across metrics and potentially impacting the robustness of our findings. Future studies could benefit from employing shorter imaging protocols, such as Magnetic Resonance Fingerprinting (MRF)[43,44], to reduce scan time and minimize the potential for motion artifacts, thereby improving patient comfort and data consistency.

Second, the heterogeneous nature of our cohort, encompassing a wide range of disease stages, ages, and cognitive statuses, introduces additional variability into our analysis. This diversity, while offering a broad perspective on PD, may introduce confounding factors that could interact with our results. To mitigate this issue, future studies with larger, stratified datasets could enable more detailed analyses of specific PD stages and subtypes, such as tremor-dominant and non-tremor-dominant groups, to assess potential differences in the spatial patterns and magnitudes of imaging parameters. Given that studies suggest greater involvement of the nigrostriatal pathway in non-tremor-dominant PD[45,46], such investigations may offer further insight into the clinical variability observed in PD.

Another challenge lies in the resolution discrepancies among qMRI metrics which pose challenges for direct comparisons. While most qMRI maps were acquired with a resolution of 1 mm, the DTI and R2 measurements were obtained at coarser resolutions of 1.5 mm and 2 mm, respectively. This variation in resolution limits the statistical comparability between parameters and may affect the interpretation of spatial gradients and their pathological significance.

In addition, while WF aims to quantify the physical fraction of water in the tissue, different calibration methods, based on CSF proton density, are applied and can lead to differences in absolute values and between-subject comparisons. Consequently, analyses relying on absolute WF values may be influenced by the chosen calibration method and its associated inherent error. To mitigate potential calibration-related biases, we compared two different WF calibration methods. We prioritized results that remained robust across methods or did not depend on absolute values, such as within-subject spatial change and within-subject asymmetry. Results that depended on the calibration method were taken cautiously and are reported in the Supplementary Materials.

Furthermore, our study employs a cross-sectional design to explore PD-related variations in biophysical properties and their correlation with behavioral variability. Future research should consider a longitudinal approach to examine how these biophysical anomalies evolve over time on the same patients and assess their potential predictive power regarding motor disability. Additionally, validating this approach across different stages of PD, from de novo to advanced stages, could provide valuable insights into the progression of these biophysical changes and their relationship with disease advancement.

Finally, while our current study focuses on the putamen as a key region in PD, we recognize the importance of extending this multimodal approach to the broader basal ganglia and nigrostriatal system, including regions such as the substantia nigra, globus pallidus, the caudate nucleus, and associated white-matter tracts. To this end, we have initiated a follow-up study that includes additional regions along this pathway, and specifically the substantia nigra[47]. This and future studies could provide further insights into the mechanisms underlying PD progression and symptom heterogeneity by studying these interconnected regions as a system.

In conclusion, our study leverages multiparametric qMRI to elucidate biophysical changes in PD, offering new insights into its neuropathology and clinical features. By providing a detailed analysis of the putamen's biophysical properties, we have identified potential biomarkers for disease detection and manifestation. Our findings underscore the importance of a comprehensive imaging approach to capture subtle, spatially dependent biological alterations in PD. The ability to quantitatively measure biophysical changes in a progressive disease like PD, presents opportunities for monitoring disease progression during studies evaluating potential disease-modifying therapies. Future research may benefit from exploring the heterogeneity within PD populations, ultimately contributing to more personalized and effective diagnostic and therapeutic strategies.

Methods

Subjects

A total of 105 PD and HC individuals participated in the study. PD patients were diagnosed based on the Movement Disorder Society Clinical Diagnostic Criteria for Parkinson's disease (MDS-PD Criteria)[48]. Two healthy subjects were excluded due to age mismatch, and two subjects were removed because of observed structural brain abnormalities that prevented reasonable segmentations of the regions for analysis. Not all participants completed all the imaging sessions. Visual inspection for quality assurance was conducted for each scan, and 11 subjects were excluded due to significant head motion that particularly affected the putamen region. Following this data screening process, the final analyses included 90 subjects: 62 PD patients and 28 HC subjects. All study procedures were approved by the Helsinki Ethics Committee of Shaare Zedek Medical Center, Jerusalem, Israel. A written informed consent was obtained from all participants before the procedure.

Behavioral assessments

Motor function and asymmetry. PD and HC participants were assessed through MDS-UPDRS III[49]. Three patients did not have the MDS-UPDRS data and were excluded from related analyses. The motor signs asymmetry score of each subject was calculated by subtracting the total score of right body-side items from the left body-side items (L-R). A higher positive score indicates left-side predominance, while a higher negative score indicates right-side predominance.

For patients exhibiting left-side predominance, the Most Affected Side (MAS) was identified as the left side of the body and the contralateral (right) putamen, while the Less Affected Side (LAS) was identified as the right side of the body and the left putamen. Conversely, for those with right-side predominance, the MAS and LAS definitions were reversed. Patients displaying no motor asymmetry were not included in analyses that compared MAS with LAS.

Cognitive assessments. The cognitive condition of PD patients and HC was evaluated using the Montreal Cognitive Assessment (MoCA)[50]. Two patients did not have MoCA data. Patients' scores ranged from 11 to 29, with mean ± SD of 23.2 ± 4.0. Among the patients, 35% fell within normal range (scores between 26 and 30), 55% exhibited mild cognitive impairment (scores between 18 and 25), and 10% were identified as having moderate cognitive impairment (scores between 10 and 17). No patients were found to have severe cognitive impairment (scores under 10).

Data acquisition

Data were collected on a 3 T Siemens MAGNETOM Skyra scanner at the Edmond and Lily Safra Center (ELSC) neuroimaging unit at the Hebrew University of Jerusalem.

R1, WF, R2* mapping. For quantitative R1, R2*, and WF mappings, 3D Fast Low Angle Shot (FLASH) images were acquired at four different flip angles ($\alpha = 4°, 10°, 20°$, and $30°$). Each image included five equally spaced

echoes, with echo time (TE) of 3.34, 6.01, 8.68, 11.35, and 14.02 ms. The repetition time (TR) was 19 ms, and the scan resolution was 1 mm^3 isotropic. To estimate the transmit field bias (B1 +), spin-echo inversion recovery (SEIR) images were acquired with echo-planar imaging readout (EPI). Imaging parameters included: TE = 49 ms, TR = 2920 ms, and inversion times (TI) of 200, 400, 1200, and 2400 ms. Slice thickness was 3 mm, and in-plane resolution was 2 mm^2.

A total of 88 subjects successfully completed the FLASH scans (60 PD and 28 HC). From those, 83 subjects also completed the SEIR scans (55 PD and 28 HC).

Whole-brain R1 and WF maps, along with estimations of transmit (B1 +) and receive (B1 −) field biases for correction, as well as a synthetic T1w image were computed from the FLASH and SEIR images, using mrQ software (https://github.com/mezera/mrQ/)[28,51].

WF mapping involves a calibration step that normalizes proton density values to the estimated pure water proton density in the ventricular CSF. To ensure the robustness of our findings across different calibration approaches, we tested two methods. The first method utilizes the median proton density values of ventricular voxels within relevant T1 value range (4.2–4.7 sec), as implemented in the mrQ software. The second method relies on the linear relationship between T1 and proton density in ventricular voxels, as recently proposed[52]. While our primary analyses use the median-based normalization, we also assessed results using both methods to evaluate consistency. Unless otherwise noted, all WF results reported in this study were consistent across both calibration methods.

R2* maps were fitted from the FLASH scans using the MPM toolbox[53]. R2* estimates acquired from each of the four FLASH images were averaged for increased signal-to-noise ratio (SNR).

MTsat. For quantitative MTsat mapping, a 3D FLASH image was acquired with an additional MT pulse, at flip angle α = 10°. The image was acquired at five equally spaced echoes (TE = 3.34 to 14.02 ms) and TR = 37 ms. Scan resolution was 1 mm^3 isotropic.

A total of 80 subjects successfully completed the MT scans (52 PD and 28 HC).

Whole-brain MTsat maps were computed from the shortest echo (3.34 ms), as described in Helms et al.[27].

DTI. For DTI measurements, diffusion-weighted spin-echo echo-planar (EPI) images were acquired, with TE = 95.8 ms and TR = 6000 ms. The diffusion weighting gradients were set in 64 directions with a diffusion weighting strength of b = 2000 s/mm^2 (G = 45mT/m, δ = 32.25 ms, Δ = 52.02 ms). Eight non-diffusion-weighted images (b = 0) were interspersed between the diffusion-weighted images. In addition, non-diffusion-weighted images with reversed phase-encoding (PE) blips were acquired. Scan resolution was 1.5 mm^3 isotropic.

A total of 68 subjects successfully completed the DTI scans (45 PD and 23 HC).

Diffusion analysis was conducted using the FMRIB's Diffusion Toolbox (FDT)[54] within FSL[55]. Corrections for distortions induced by susceptibility and eddy currents were performed using the reverse PE data, utilizing the EDDY[56] and TOPUP[57] functions. After correction, MD and FA maps were generated using the DTIFIT function in FDT.

QSM. Multi-echo gradient echo images were acquired at seven echoes (TE = 8.41, 14.04, 18.86, 22.45, 26.28, 30.89, and 35.52 ms), TR = 41 ms, and flip angle of α = 15°. Scan resolution was 1 mm^3 isotropic.

QSM processing utilized Tikhonov regularization-based estimation[58], and using the Morphology Enabled Dipole Inversion (MEDI) toolbox[59]. This included frequency offset calculation for each voxel via complex fitting, spatial phase unwrapping, and background field removal.

Out of 62 participants who underwent susceptibility imaging, 14 were excluded from the final analysis because of substantial acquisition artifacts, resulting in a total of 48 subjects (23 PD and 25 HC).

R2. For quantitative T2 mapping, multi-echo spin echo images were acquired at 10 equally spaced echoes between 12 ms and 120 ms, and TR = 4210 ms. Scan resolution was 2 mm^3 isotropic.

Whole-brain R2 (1/T2) maps were fitted using the nine longest TEs (shortest TE = 12 ms was excluded), by solving the following T2-weighted signal (S) equation[60], simultaneously for T2 and M0:

$$S = M0 * \exp\left(-\frac{TE}{T2}\right) \quad (1)$$

A total of 61 subjects successfully completed the T2 scans (34 PD and 27 HC).

Regions of Interest (ROIs)

Putamen ROIs were delineated using FSL's FIRST probabilistic segmentation tool[61]. The subject's synthetic T1w image was used as a reference image. To minimize partial volume effects, the outer 1-mm layer of the ROIs were removed. Visual inspection of all segmented ROIs was conducted to ensure quality. The segmentation was transformed also to the R2 space (2 mm^3) and the DTI space (1.5 mm^3). For R2, a rigid body transformation from R1 to R2 was computed using SPM (www.fil.ion.ucl.ac.uk/spm/software/spm12/) and was then applied on the segmentation volume. In the case of DTI, a nonlinear transformation from R1 to FA was performed using ANTS[62], and was then applied on the segmentation.

Putamen AP gradients

We computed qMRI gradients along the putamen's major (AP) axis as described in Drori et al.[11], using the mrGrad toolbox (https://github.com/MezerLab/mrGrad/). In short, the major axis of the putamen structure is computed using singular value decomposition (SVD) of the ROI coordinates, independently of the image axis system and image intensities. The image values (i.e., the qMRI parameter) were then sampled along the axis, as the median value of each equally-spaced segment along the axis. In our study we used 20 equally spaced segments along the AP axis. The obtained values represent a spatial function of the sampled parameter along the axis. We then smoothed the profile using a moving gaussian kernel of size 5.

Interhemispheric asymmetry

We defined interhemispheric asymmetry on the subject level as the left-hemisphere value (in an ROI or a gradient node) minus the right-hemisphere value. With this definition, a negative value reflects a higher value in the right hemisphere, and a positive value reflects a higher value in the left hemisphere.

Tissue- and iron-relaxivity frameworks

To Investigate variations in macromolecular composition and iron homeostasis in the PP, we applied the in vivo Tissue- and Iron-Relaxivity frameworks proposed by Filo et al.[26,31] (https://github.com/shirfilo/MDM_toolbox and https://github.com/shirfilo/r1_r2s_rel_toolbox). In short, the linear dependencies of R1 on the non-water fraction (dR1/d(1-WF); i.e., Tissue-Relaxivity) and on R2* (dR1/dR2*; i.e., Iron-Relaxivity), were calculated to detect variations in the macromolecular composition and iron homeostasis, respectively, rather than changes in quantities of tissue and iron. Values of 1-WF or R2* were binned into 36 equally spaced intervals prior to the linear regression analysis. The linear fitting was done within the PP mask, defined post hoc as the posterior segments where significant differences were found between PD and HC in WF.

Linear mixed-effects statistical models

Statistical inference for spatial and disease-related effects was performed using linear mixed-effects models (LMMs).

For each MRI metric, the position along the putamen AP axis (20 interval levels from 0.00 to 1.00), and the clinical group (two categorical levels: PD, HC), were included as fixed effects. In addition, Age and Sex were included as covariates. Subject ID was included as a random effect, and the

MRI metric served as the dependent variable:

$$MRI \sim Position \times Clinical\ Group + Age + Sex + (1|Subject\ ID) \quad (2)$$

For supplementary evaluation of quadratic spatial effects, we also integrated a quadratic position term:

$$MRI \sim Position \times Clinical\ Group + Position^2 \times Clinical\ Group + Age + Sex + (1|Subject\ ID) \quad (3)$$

Standardized beta coefficients (β) were computed by z-scoring all continuous variables, including Age and the MRI response variables. Position was not z-scored as it was already normalized between 0 and 1, allowing $\beta_{Position}$ to represent the estimated change along the entire AP axis of the putamen. The P values reported in this article were corrected for multiple comparisons using the Benjamini-Hochberg method for false discovery rate (BH-FDR)[63].

Post hoc power analysis for LMM effects

To evaluate whether the sample size in each analysis was sufficient to detect the effects of Position and its interaction with Clinical Group, we conducted a post hoc power analysis, following the methodology described by Cohen[64] based on the actual effect sizes (partial eta-squared, η^2) estimated from our LMMs. We used η^2 values from the fitted models and the effective sample size derived from the data to account for group imbalance. The effect size (η^2) for both the main effect of Position and its interaction with Clinical Group was computed from the F-statistic and degrees of freedom (DF) obtained using ANOVA on the LMM model:

$$\eta^2 = \frac{F \times DF_1}{F \times DF_1 + DF_2} \quad (4)$$

where F is the F-statistic for the effect, DF_1 is the degrees of freedom for the effect, and DF_2 is the residual degrees of freedom. Since the groups were unbalanced, we computed the effective sample size using the harmonic mean of the group sizes:

$$\mathbf{N}_{\mathbf{effective}} = \frac{\mathbf{2} \times \boldsymbol{N_{PD}} \times \boldsymbol{N_{HC}}}{\boldsymbol{N_{PD}} + \boldsymbol{N_{HC}}} \quad (5)$$

This method accounts for the imbalance by adjusting the total sample size to reflect its statistical power equivalence in a balanced design. We computed the statistical power based on the effect's F-statistic, the effect size (η^2), and the effective sample size. Power was estimated following the methodology of Cohen[64], using the non-central F-distribution, which determines the probability of rejecting the null hypothesis given the observed effect size. Specifically, power was calculated as:

$$Power = 1 - P\left(F_{crit}, DF_1, DF_2, \lambda\right) \quad (6)$$

where $P\left(F_{crit}, DF_1, DF_2, \lambda\right)$ is the cumulative probability of the non-central F-distribution under the null hypothesis, F_{crit} is the critical F-value for the given $\alpha = 0.05$ threshold, and $\lambda = \eta^2 \times DF_2$ is the non-centrality parameter that adjusts the test for the observed effect size.

Post hoc analysis for localization of Group × Position interactions

As a post hoc analysis to identify specific positions where group differences in gradient effects were most pronounced, we refitted the linear mixed-effects models treating Position as a categorical variable rather than a continuous one. This approach allowed us to estimate separate interaction coefficients for Clinical Group × Position at each of the 20 interval levels along the putamen AP axis, obtaining individual coefficient estimates at each position. For each MRI metric, we identified the position with the largest and/or statistically significant interaction effect (corrected for multiple comparisons using BH-FDR), highlighting spatial locations where group differences were strongest. This analysis also provided a means to assess the robustness of localized effects across multiple MRI parameters, helping to determine whether certain positions consistently exhibited prominent disease-related differences. The model structure remained unchanged, with Age and Sex as covariates and Subject ID as a random effect. This categorical approach offered a more detailed characterization of the spatial distribution of group differences in MRI metrics.

Group comparisons

For the analyses in this study requiring comparisons between two independent groups or within a single group, appropriate statistical tests were selected based on assumption checks. Normality was assessed using the Shapiro-Wilk test, and homogeneity of variances (for between-group comparisons) was tested with Levene's test. In supplementary volumetric and whole-ROI analyses, assumptions for parametric testing were met, and two-sample t-tests were used. For the Relaxivity analysis normality was violated, and the non-parametric Mann-Whitney U test was applied instead. For the within-subject LAS-MAS comparisons, normality was confirmed, allowing the use of paired t-tests. Since the LAS-MAS comparisons were conducted at multiple positional levels along the AP axis, multiple comparison correction was applied using the Nichols and Holmes permutation test, which appropriately accounts for the dependence among positional levels[65].

PD-related variable correlations

To test the relationships between the putamen's gradient asymmetry and the motor function asymmetry, we fitted linear regression models. We report R^2 values, representing the proportion of variance explained by the structural asymmetry variable. To rule out effects of age and sex, we added these variables as covariates in the regression models.

Data availability

The qMRI dataset supporting the findings of this study can be provided by A.A.M. pending scientific review and a completed material transfer agreement. Requests should be submitted to aviv.mezer@mail.huji.ac.il.

Code availability

The main gradient analysis tool used in this study is available at https://github.com/MezerLab/mrGrad/. All analysis scripts are available from the corresponding author upon reasonable request.

Received: 15 August 2024; Accepted: 2 May 2025;
Published online: 03 July 2025

References

1. Tolosa, E., Wenning, G. & Poewe, W. The diagnosis of Parkinson's disease. *Lancet Neurol.* **5**, 75–86 (2006).
2. Redgrave, P. et al. Goal-directed and habitual control in the basal ganglia: Implications for Parkinson's disease. *Nat. Rev. Neurosci.* **11**, 760–772 (2010).
3. Calabresi, P., Picconi, B., Parnetti, L. & Di Filippo, M. A convergent model for cognitive dysfunctions in Parkinson's disease: the critical dopamine-acetylcholine synaptic balance. *Lancet Neurol.* **5**, 974–983 (2006).
4. Surmeier, D. J., Obeso, J. A. & Halliday, G. M. Selective neuronal vulnerability in Parkinson disease. *Nat. Rev. Neurosci.* **18**, 101–113 (2017).
5. Zucca, F. A. et al. Interactions of iron, dopamine and neuromelanin pathways in brain aging and Parkinson's disease. *Prog. Neurobiol.* **155**, 96–119 (2017).
6. Kaasinen, V. & Vahlberg, T. Striatal dopamine in Parkinson disease: A meta-analysis of imaging studies. *Ann. Neurol.* **82**, 873–882 (2017).
7. Jeong, E. H., Lee, J. Y. & Song, Y. S. Longitudinal Serotonergic and Dopaminergic Binding: Impact on Parkinson's Disease Progression and Levodopa Dyskinesia. *J. Neuroimaging* **35**, e70014 (2025).

8. Yang, Z., Xie, Y., Dou, K., Yang, L. & Xie, A. Associations of striatal dopamine transporter binding with motor and non-motor symptoms in early Parkinson's disease. *Clin. Transl. Sci.* **16**, 1021–1038 (2023).
9. Kish, S. J., Shannak, K. & Hornykiewicz, O. Uneven Pattern of Dopamine Loss in the Striatum of Patients with Idiopathic Parkinson's Disease. *N. Engl. J. Med.* **318**, 876–880 (1988).
10. Politis, M. Neuroimaging in Parkinson disease: from research setting to clinical practice. *Nat. Rev. Neurol.* **10**, 708–722 (2014).
11. Drori, E., Berman, S. & Mezer, A. A. Mapping microstructural gradients of the human striatum in normal aging and Parkinson's disease. *Sci Adv* **8**, eabm1971 (2022).
12. Graybiel, A. M. & Ragsdale, C. W. Histochemically distinct compartments in the striatum of human, monkeys, and cat demonstrated by acetylthiocholinesterase staining. *Proc. Natl Acad. Sci.* **75**, 5723–5726 (1978).
13. Haber, S. N. Corticostriatal circuitry. *Dialogues Clin. Neurosci.* **18**, 7–21 (2016).
14. De Barros, A. et al. Iron distribution in the lentiform nucleus: A post-mortem MRI and histology study. *Brain Struct. Funct.* **226**, 351–364 (2021).
15. Draganski, B. et al. Evidence for segregated and integrative connectivity patterns in the human basal ganglia. *J. Neurosci.* **28**, 7143–7152 (2008).
16. Mestres-Missé, A., Turner, R. & Friederici, A. D. An anterior-posterior gradient of cognitive control within the dorsomedial striatum. *Neuroimage* **62**, 41–47 (2012).
17. Manza, P., Zhang, S., Li, C.-S. R. & Leung, H.-C. Resting-state functional connectivity of the striatum in early-stage Parkinson's disease: Cognitive decline and motor symptomatology. *Hum. Brain Mapp.* **37**, 648–662 (2016).
18. Tian, Y., Margulies, D. S., Breakspear, M. & Zalesky, A. Topographic organization of the human subcortex unveiled with functional connectivity gradients. *Nat. Neurosci.* **23**, 1421–1432 (2020).
19. Peters, A. J., Fabre, J. M. J., Steinmetz, N. A., Harris, K. D. & Carandini, M. Striatal activity topographically reflects cortical activity. *Nature* **591**, 420–425 (2021).
20. Marquand, A. F., Haak, K. V. & Beckmann, C. F. Functional corticostriatal connection topographies predict goal-directed behaviour in humans. *Nat. Hum. Behav.* **1**, 1–9 (2017).
21. O'Rawe, J. F., Ide, J. S. & Leung, H. C. Model testing for distinctive functional connectivity gradients with resting-state fMRI data. *Neuroimage* **185**, 102–110 (2019).
22. Weiskopf, N., Mohammadi, S., Lutti, A. & Callaghan, M. F. Advances in MRI-based computational neuroanatomy: From morphometry to in-vivo histology. *Curr. Opin. Neurol.* **28**, 313–322 (2015).
23. Weiskopf, N., Edwards, L. J., Helms, G., Mohammadi, S. & Kirilina, E. Quantitative magnetic resonance imaging of brain anatomy and in vivo histology. *Nat. Rev. Phys.* **3**, 570–588 (2021). *2021 3:8*.
24. Pyatigorskaya, N., Gallea, C., Garcia-Lorenzo, D., Vidailhet, M. & Lehericy, S. A review of the use of magnetic resonance imaging in Parkinson's disease. *Ther. Adv. Neurol. Disord.* **7**, 206–220 (2014).
25. Deistung, A. et al. Toward in vivo histology: A comparison of quantitative susceptibility mapping (QSM) with magnitude-, phase-, and R2*-imaging at ultra-high magnetic field strength. *Neuroimage* **65**, 299–314 (2013).
26. Filo, S. et al. Non-invasive assessment of normal and impaired iron homeostasis in the brain. *Nat. Commun.* **14**, 1–19 (2023).
27. Helms, G., Dathe, H., Kallenberg, K. & Dechent, P. High-resolution maps of magnetization transfer with inherent correction for RF inhomogeneity and T1 relaxation obtained from 3D FLASH MRI. *Magn. Reson Med* **60**, 1396–1407 (2008).
28. Mezer, A. et al. Quantifying the local tissue volume and composition in individual brains with magnetic resonance imaging. *Nat. Med* **19**, 1667–1672 (2013).
29. Pierpaoli, C. & Basser, P. J. Toward a quantitative assessment of diffusion anisotropy. *Magn. Reson Med* **36**, 893–906 (1996).
30. Le Bihan, D. Looking into the functional architecture of the brain with diffusion MRI. *Nat. Rev. Neurosci.* **4**, 469–480 (2003).
31. Filo, S. et al. Disentangling molecular alterations from water-content changes in the aging human brain using quantitative MRI. *Nat. Commun.* **10**, 3403 (2019).
32. Mullin, S. et al. Ambroxol for the Treatment of Patients With Parkinson Disease With and Without Glucocerebrosidase Gene Mutations: A Nonrandomized, Noncontrolled Trial. *JAMA Neurol.* **77**, 427–434 (2020).
33. Aviles-Olmos, I. et al. Motor and Cognitive Advantages Persist 12 Months After Exenatide Exposure in Parkinson's Disease. *J. Parkinsons Dis.* **4**, 337–344 (2014).
34. Athauda, D. et al. Exenatide once weekly versus placebo in Parkinson's disease: a randomised, double-blind, placebo-controlled trial. *Lancet* **390**, 1664–1675 (2017).
35. Oestreich, L. K. L. & O'Sullivan, M. J. Transdiagnostic In Vivo Magnetic Resonance Imaging Markers of Neuroinflammation. *Biol. Psychiatry Cogn. Neurosci. Neuroimaging* **7**, 638–658 (2022).
36. Loeffler, D. A. et al. Transferrin and Iron in Normal, Alzheimer's Disease, and Parkinson's Disease Brain Regions. *J. Neurochem* **65**, 710–716 (1995).
37. Ulla, M. et al. Is R2* a New MRI Biomarker for the Progression of Parkinson's Disease? A Longitudinal Follow-Up. *PLoS One* **8**, e57904 (2013).
38. Chougar, L. et al. Comparison of mean diffusivity, R2* relaxation rate and morphometric biomarkers for the clinical differentiation of parkinsonism. *Parkinsonism Relat. Disord.* **108**, 105287 (2023).
39. Barbosa, J. H. O. et al. Quantifying brain iron deposition in patients with Parkinson's disease using quantitative susceptibility mapping, R2 and R2*. *Magn. Reson Imaging* **33**, 559–565 (2015).
40. Ryvlin, P. et al. Magnetic Resonance Imaging Evidence of Decreased Putamenal Iron Content in Idiopathic Parkinson's Disease. *Arch. Neurol.* **52**, 583–588 (1995).
41. Langkammer, C. et al. Quantitative Susceptibility Mapping in Parkinson's Disease. *PLoS One* **11**, e0162460 (2016).
42. Bagnato, F. et al. Untangling the R2* contrast in multiple sclerosis: A combined MRI-histology study at 7.0 Tesla. *PLoS One* **13**, e0193839 (2018).
43. Ma, D. et al. Magnetic resonance fingerprinting. *Nature* **495**, 187–192 (2013).
44. Cao, X. et al. DTI-MR fingerprinting for rapid high-resolution whole-brain T1, T2, proton density, ADC, and fractional anisotropy mapping. *Magn. Reson Med* **91**, 987–1001 (2024).
45. Selikhova, M. et al. A clinico-pathological study of subtypes in Parkinson's disease. *Brain* **132**, 2947–2957 (2009).
46. Boonstra, J. T., Michielse, S., Temel, Y., Hoogland, G. & Jahanshahi, A. Neuroimaging Detectable Differences between Parkinson's Disease Motor Subtypes: A Systematic Review. *Mov. Disord. Clin. Pr.* **8**, 175 (2020).
47. Drori, E. & Mezer, A. A. Motor Signs in Parkinson's Disease are Explained by Substantia Nigra and Putamen Asymmetries. in *OHBM 2023 Annual Meeting* (2023).
48. Postuma, R. B. et al. MDS clinical diagnostic criteria for Parkinson's disease. *Mov. Disord.* **30**, 1591–1601 (2015).
49. Goetz, C. G. et al. Movement Disorder Society-sponsored revision of the Unified Parkinson's Disease Rating Scale (MDS-UPDRS): Scale presentation and clinimetric testing results. *Mov. Disord.* **23**, 2129–2170 (2008).
50. Nasreddine, Z. S. et al. The Montreal Cognitive Assessment, MoCA: A Brief Screening Tool For Mild Cognitive Impairment. *J. Am. Geriatr. Soc.* **53**, 695–699 (2005).
51. Mezer, A., Rokem, A., Berman, S., Hastie, T. & Wandell, B. A. Evaluating quantitative proton-density-mapping methods. *Hum. Brain Mapp.* **37**, 3623–3635 (2016).
52. Mama, E., Marques, J. P. & Mezer, A. A. A new approach for reproducible water fraction and T1 mapping across different qMRI

acquisition protocols. in *2024 ISMRM & ISMRT Annual Meeting & Exhibition* (Singapore, 2024).
53. Weiskopf, N. et al. Quantitative multi-parameter mapping of R1, PD*, MT, and R2* at 3T: a multi-center validation. *Front. Neurosci.* **7**, 95 (2013).
54. Behrens, T. E. J. et al. Characterization and Propagation of Uncertainty in Diffusion-Weighted MR Imaging. *Magn. Reson. Med.* **50**, 1077–1088 (2003).
55. Smith, S. M. et al. Advances in functional and structural MR image analysis and implementation as FSL. *Neuroimage* **23**, S208–S219 (2004).
56. Andersson, J. L. R. & Sotiropoulos, S. N. An integrated approach to correction for off-resonance effects and subject movement in diffusion MR imaging. *Neuroimage* **125**, 1063–1078 (2016).
57. Andersson, J. L. R., Skare, S. & Ashburner, J. How to correct susceptibility distortions in spin-echo echo-planar images: application to diffusion tensor imaging. *Neuroimage* **20**, 870–888 (2003).
58. Karsa, A., Punwani, S. & Shmueli, K. An optimized and highly repeatable MRI acquisition and processing pipeline for quantitative susceptibility mapping in the head-and-neck region. *Magn. Reson Med* **84**, 3206–3222 (2020).
59. Liu, J. et al. Morphology enabled dipole inversion for quantitative susceptibility mapping using structural consistency between the magnitude image and the susceptibility map. *Neuroimage* **59**, 2560–2568 (2012).
60. Dowell, N. G. & Wood, T. C. T2: Transverse Relaxation Time. in *Quantitative MRI of the brain: principles of physical measurement* (eds. Cercignani, M., Dowell, N. G. & Tofts, P. S.) 83–96 (CRC Press, 2018). https://doi.org/10.1201/B21837-6.
61. Patenaude, B., Smith, S. M., Kennedy, D. N. & Jenkinson, M. A Bayesian model of shape and appearance for subcortical brain segmentation. *Neuroimage* **56**, 907–922 (2011).
62. Avants, B. B., Tustison, N. & Song, G. Advanced normalization tools (ANTS). *Insight J* **2**, 1–35 (2009).
63. Benjamini, Y. & Hochberg, Y. Controlling the False Discovery Rate: A Practical and Powerful Approach to Multiple Testing. *J. R. Stat. Soc.: Ser. B (Methodol.)* **57**, 289–300 (1995).
64. Cohen, J. Statistical Power Analysis for the Behavioral Sciences. *Statistical Power Analysis for the Behavioral Sciences* (2013) https://doi.org/10.4324/9780203771587.
65. Nichols, T. E. & Holmes, A. P. Nonparametric permutation tests for functional neuroimaging: A primer with examples. *Hum. Brain Mapp.* **15**, 1–25 (2002).

Acknowledgements

This research was financially supported by the NOFAR program of the Israel Innovation Authority and Teva Pharmaceuticals, and by the Israel Science Foundation (grants no. 1169/20 and 2449/24) given to AAM. We thank S. Filo and S. Moskovich for their critical reading of the manuscript and their useful comments.

Author contributions

E.D. and A.A.M. conceived the study and drafted the manuscript. E.D. developed the algorithms, wrote the code, and designed the figures. G.Y., L.C., and D.A. recruited human participants. E.D., A.A.M., and L.C. acquired the imaging data. G.Y. performed the clinical assessments and collected demographic data. L.C., G.Y., and D.A. critically revised the manuscript and contributed to the interpretation of study results.

Competing interests

The Hebrew University of Jerusalem filed PCT Patent Application No. PCT/IL2021/050762, titled “System and method for using medical imaging devices to perform non-invasive diagnosis of a subject”, on 22 June 2021. This patent concerns the gradient method described in this paper.

Additional information

Supplementary information The online version contains supplementary material available at https://doi.org/10.1038/s41531-025-01020-0.

Correspondence and requests for materials should be addressed to Elior Drori.